



# Dual-energy CT: theoretical principles and clinical applications

Andrea Agostini<sup>1,2</sup> · Alessandra Borgheresi<sup>2</sup> · Alberto Mari<sup>3</sup> · Chiara Floridi<sup>4</sup> · Federico Bruno<sup>5</sup> · Marina Carotti<sup>2</sup> · Nicolò Schicchi<sup>2</sup> · Antonio Barile<sup>5</sup> · Stefania Maggi<sup>3</sup> · Andrea Giovagnoni<sup>1,2</sup>

Received: 11 October 2019 / Accepted: 13 November 2019 / Published online: 2 December 2019  
© Italian Society of Medical Radiology 2019

## Abstract

The physical principles of dual-energy computed tomography (DECT) are as old as computed tomography (CT) itself. To understand the strengths and the limits of this technology, a brief overview of theoretical basis of DECT will be provided. Specific attention will be focused on the interaction of X-rays with matter, on the principles of attenuation of X-rays in CT toward the intrinsic limits of conventional CT, on the material decomposition algorithms (two- and three-basis-material decomposition algorithms) and on effective Rho-Z methods. The progresses in material decomposition algorithms, in computational power of computers and in CT hardware, lead to the development of different technological solutions for DECT in clinical practice. The clinical applications of DECT are briefly reviewed in relation to the specific algorithms.

## List of symbols

$\sigma$	Cross section, or the probability of interaction photon–electron
$R$	Rayleigh scattering
$\tau$	Photoelectric absorption
$K, L$	Inner electron shells
$Z$	Atomic number
$E$	Energy
$k$	Constant
$\rho$	Physical density
$A$	Atomic weight
$h$	Plank’s constant
$\nu$	Speed of photon
$\propto$	Proportional to
$c$	Compton scattering

$n_e$	Electron density
$I$	Intensity
$x$	Thickness
$e$	Euler’s number or Napier’s constant
CT#	CT number in Hounsfield’s units
$\mu/\rho$	Mass attenuation coefficient
$\sum$	Summation of multiple terms
$\approx$	Approximately equal to
$\alpha$	Constant in Eq. 8
$\beta$	Constant in Eq. 8
$d$	Exponent in Eq. 8
$g$	Exponent in Eq. 8
$f_{KN}(E)$	Klein–Nishina function
$\rho Z$ and <i>Rho-Z</i>	Material decomposition method using effective density and atomic numbers
$r$	Spatial location of the unit volume
$\rho_i$	Physical density of the <i>i</i> th basis material
$\delta_i$	Area density of the <i>i</i> th basis material
$V_i$	Fractional volume of the <i>i</i> th basis material
$m_i$	Fractional mass of the <i>i</i> th basis material

✉ Andrea Agostini  
dott.andrea.agostini@gmail.com

<sup>1</sup> Department of Clinical, Special and Dental Sciences, University Politecnica delle Marche, Ancona, Italy

<sup>2</sup> Department of Radiology – Division of Special and Pediatric Radiology, University Hospital “Umberto I – Lancisi – Salesi”, Via Conca 71, 60126 Ancona, AN, Italy

<sup>3</sup> Department of Radiology – Division of Medical Physics, University Hospital “Umberto I – Lancisi – Salesi”, Via Conca 71, 60126 Ancona, AN, Italy

<sup>4</sup> Department of Health Sciences, Diagnostic and Interventional Radiology, Hospital “San Paolo”, University of Milan, Milan, Italy

<sup>5</sup> Department of Biotechnological and Applied Sciences, University of L’Aquila, Via Vetoio 1, 67100 L’Aquila, Italy

## Abbreviations

DECT	Dual-energy CT
CT	Computed tomography
$Z$	Atomic number
dsDECT	Dual-source dual-energy CT
VMI	Virtual monoenergetic images
FOV	Field of view
VNC	Virtual non-contrast
MRI	Magnetic resonance imaging
VR	Volume rendering

## Introduction

“...It is possible to use the machine for determining approximately the atomic number of the material within the slice. Two pictures are taken of the same slice, one at 100 kV and the other at 140 kV. ... One picture can then be subtracted from the other by the computer so that areas containing high atomic numbers can be enhanced. ... For example, tests carried out to date have shown that iodine ( $Z=53$ ) can be readily distinguished from Calcium ( $Z=20$ ). ...” [1]. Sir G.N. Hounsfield while describing his new computerized axial tomography system observed that elements with atomic number ( $Z$ ) can be easily recognized and distinguished one each other. This was the first empirical observation of material decomposition in computed tomography (CT) opening a new research field: material decomposition in dual-energy computed tomography (DECT) [2, 3]. This technology remained secondary to conventional CT until 2005, with the introduction of the dual-source DECT (dsDECT) [4]. In the following years, several technologies have been developed and the applications of DECT are more widely spread in the clinical routine.

This review will provide a brief overview on theoretical principles behind DECT (better understood after reviewing the interactions of X-rays with matter), the available technologies and the main clinical applications.

## X-rays: interaction with matter

The polychromatic spectrum (photons with different wavelengths and energies) of X-rays produced by the tube interacts and exchange energy with the biological matter with a combination of several phenomena: Rayleigh scattering, photoelectric absorption, Compton scattering, and pair production. The probability of each of them, expressed as cross section ( $\sigma$ ), is related to the energy of the incident photon and properties of the material [5]. The Rayleigh scattering ( $R$ ) and the pair production give minor contribution to X-ray attenuation and are considered of minor relevance at energies used in CT [5].

The photoelectric absorption ( $\tau$ ) involves the electrons of the inner shells ( $K$  or  $L$ ). The energy is completely transferred from the photon to the electron which is ejected; the vacancy is filled by an electron from outer shells with emission of characteristic radiation or an Auger electron. The probability of photoelectric interaction as linear attenuation coefficient ( $\mu_\tau$ , see the next section) follows the rule:

$$\mu_\tau = k \frac{\rho Z^4}{A(h\nu)^3} \propto Z^4 E^{-3} \quad (1)$$

where  $k$  is a constant depending on the electron shell,  $\rho$  is the density,  $Z$  is the atomic number of the target,  $A$  the atomic weight,  $h$  is the Planck's constant,  $\nu$  is the speed of photon, and  $E$  is the energy of the incident photon. The photoelectric interaction greatly increases with the atomic number of the target ( $\propto Z^4$ ). When the photon energy reaches the binding energy of the electron, there is a peak in the probability of photoelectric absorption (absorption edge,  $k$ -edge if an electron in the  $k$ -shell is involved). For energies above the absorption edge, the probability of interactions rapidly decreases ( $\propto 1/E^3$ ) [5, 6].

The Compton scattering ( $c$ ) involves the electrons in the outer shell. The incident photon exchanges part of the kinetic energy with the electron; the electron is ejected, and the scattered photon continues the travel with a lower energy and a scatter angle. The probability of Compton scattering is proportional to the electron density (number of electrons per gram,  $n_e$ ), which is quite constant for most materials except for hydrogen. For most of biological tissues, the electron density is proportional physical density  $\rho$ . The probability of Compton scattering, described as linear attenuation coefficient ( $\mu_C$ ), can be approximated as proportional to the electron density and inversely proportional to the X-ray photon energy [7]:

$$\mu_C \propto n_e E^{-1} \quad (2)$$

## Limits of computed tomography (CT) and physical principles of dual-energy CT (DECT)

Experimentally, when a monochromatic (one specific energy) X-ray beam with an energy  $E$  and intensity  $I_0$  is attenuated by a homogeneous material, the residual intensity after a thickness  $x$  ( $I_x$ ) follows the Lambert–Beer's law:

$$I_x = I_0 e^{-\mu x} = I_0 e^{-\mu(\rho, Z, E)x} \quad (3)$$

where  $e$  is the Euler's or Napier's constant and the linear attenuation coefficient  $\mu$  (the fractional attenuation of the X-ray beam per unit thickness of the attenuating material) is a function of the energy of the X-ray beam ( $E$ ), the atomic number ( $Z$ ) and the physical density ( $\rho$ ) of the material [8]. In CT, the linear attenuation coefficient of each scanned voxel ( $r$ , the considered unit volume) can be derived from the CT number (CT#) in the Hounsfield's equation [1, 9]:

$$\text{CT\#} = \frac{\mu(r) - \mu_{\text{water}}}{\mu_{\text{water}}} \times 1000 \quad (4)$$

The linear attenuation coefficient is related to the physical density  $\rho$ , and its application in the attenuation of

biological tissues can be less convenient. Indeed, each unitary volume of biological tissues is composed by a mixture of different compounds present at variable relative quantities. The physical density  $\rho$  of the attenuating material is influenced by the physical state of the matter; however, the energies involved in photon–electron interactions are much greater than the energies involved in molecular bindings; thus, the linear attenuation coefficient  $\mu$  can be considered approximately proportional the physical density  $\rho$  and Eq. 3 can be written as:

$$I_x = I_0 e^{-\left[\frac{\mu(Z,E)}{\rho}\right] \rho x} \tag{5}$$

where  $\mu/\rho$  can be the mass attenuation coefficient [8]. In the case of a mixture of materials, such as biological tissues, the mass attenuation coefficient can be approximated as the sum of the mass attenuation coefficients of each compound:

$$\frac{\mu}{\rho} = \sum_i w_i \frac{\mu_i}{\rho_i} \tag{6}$$

where  $w_i$  is the weight fraction of each compound of the mixture [8]. This is the mathematical expression of the intrinsic limits of CT: considering the attenuation of a mixture with

two known materials at unknown proportions, Eq. 6 has no solution because it is an equation in two unknowns ( $w_1$  and  $w_2$ ) and one solution ( $\mu$ , or CT#) [8, 9]. Since the CT number refers to the total linear attenuation coefficient of a mixture (biological tissue) composed by different compounds at unknown densities (but known attenuation curves), it can be impossible to differentiate the different materials present in the compound (Fig. 1). It is common experience that the iodine and calcium present at different densities (concentrations) may have the same attenuation (i.e., the same CT number), such as microcalcifications in an enhancing mass (Fig. 2). However, different materials, such as iodine and calcium, have different attenuation curves (linear attenuation coefficients as function of energy), and if scanned at different energies, they can be differentiated (Figs. 1 and 2). Starting from this problem, the algorithms of material decomposition in dual-energy CT were developed [10].

Returning to Eq. 6, the mass attenuation coefficient of a given material exposed to X-ray at a given X-ray energy can be expressed as the sum of the cross sections of each attenuation phenomenon or the sum of the relative mass attenuation coefficients of each phenomenon, being the most relevant the photoelectric and the Compton interactions [8, 11, 12]:

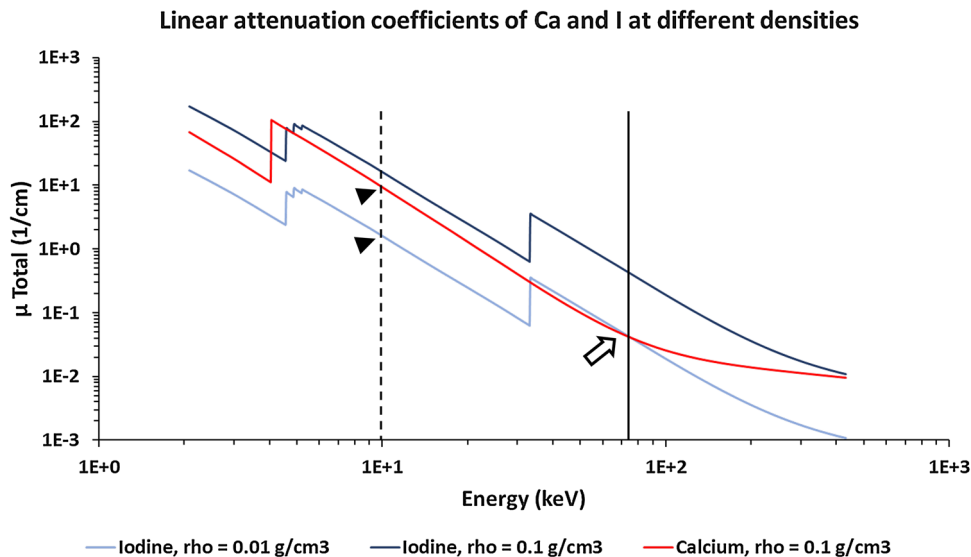


**Fig. 1** Linear attenuation coefficients, the limits of CT, and principles of dual energy CT. The plot shows the linear attenuation coefficient ( $\mu$  total) of iodine at different densities ( $\rho=0.1 \text{ g/cm}^3$ , light blue;  $\rho=0.01 \text{ g/cm}^3$ , dark blue) and calcium ( $\rho=0.1 \text{ g/cm}^3$ , red) as function of energy of the incident X-ray photon. Approximating the X-ray beam in CT to monochromatic, the colored curves are a representation of the CT numbers ( $\mu$  total) of a given material at a given density when irradiated with a given energy. The attenuation curve is characteristic of the material and models the Compton and photoelectric interactions: the blue curves of iodine at two different densities are equal with the same absorption edges; the value of linear attenuation coefficient ( $\mu$  total) is function of energy (the shape of the curve) and

of density (light and dark blue curves of iodine). If iodine at  $0.01 \text{ mg/cm}^3$  (dark blue) and calcium at  $0.1 \text{ g/cm}^3$  (red) are irradiated with an energy of  $\approx 75 \text{ keV}$  (black solid line), they will provide the same linear attenuation coefficients and thus the same CT number and can be indistinguishable (empty arrow). If the same materials at the same densities are scanned at a different energy levels (e.g.,  $10 \text{ keV}$ , black dashed line), the linear attenuation coefficients and the CT numbers are clearly different (black arrowheads). By knowing the attenuation curves, a couple of materials can be characterized and quantified if scanned at two energy levels (i.e., material decomposition in dual-energy CT). Data from the U.S. National Institute of Standards and Technology (<https://www.nist.gov/>; accessed on October 8, 2019)

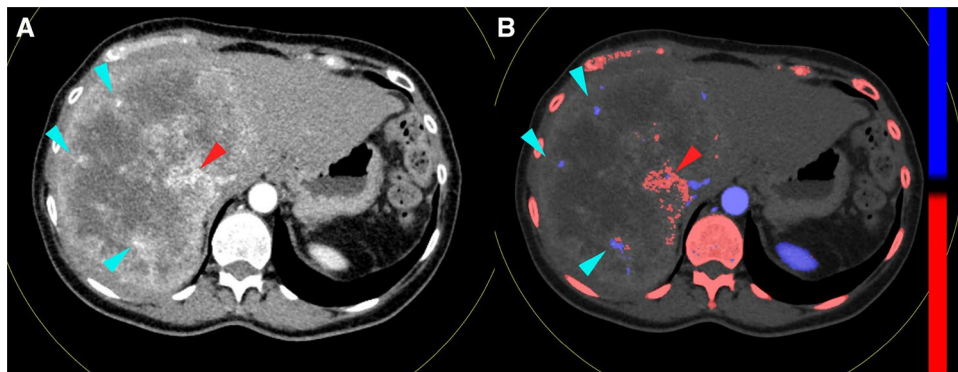


**Fig. 2** CT and dual-energy CT. Female, 58 y.o., metastasis from colorectal cancer, arterial phase. Dual-energy acquisition (third-generation dual-source CT), 90/150 Sn kVp, arterial phase. **a** Mixed image (0.5). In the mixed images, the CT numbers in each pixel are a weighted sum of the correspondent CT numbers in the low- and high-energy reconstructed images and can be considered as similar to con-

ventional CT. In **a**, the enhancing arteries within the lesion (light blue arrowheads) have density similar to intralésional calcifications (red arrowhead). **b** Material labeling. The material decomposition evaluates the different attenuation curves of the basis materials, allowing for material labeling (iodine: blue map and arrowheads; calcium: red map and arrowheads)

$$\frac{\mu}{\rho}(E) = \frac{\mu_C}{\rho}(E) + \frac{\mu_{\tau}}{\rho}(E) + \frac{\mu_R}{\rho}(E) \approx \frac{\mu_C}{\rho}(E) + \frac{\mu_{\tau}}{\rho}(E) \quad (7)$$

This principle is at the basis of the first two-basis-material decomposition algorithm developed by Alvarez and Macovski. This demonstrates that when using a conventional X-ray beam, the effective attenuation coefficient can be calculated from the contribution of Compton and photoelectric interactions modeled on the effective  $\rho_{\text{eff}}$  (density) and  $Z_{\text{eff}}$  (atomic number) of the material:

$$\begin{aligned} \frac{\mu_{\text{eff}}}{\rho_{\text{eff}}}(E) &\approx \frac{\mu_C}{\rho}(E) + \frac{\mu_{\tau}}{\rho}(E) \Rightarrow \mu_{\text{eff}}(E) \approx \rho_{\text{eff}} \left( \frac{\mu_C}{\rho}(E) + \frac{\mu_{\tau}}{\rho}(E) \right) \\ &\Rightarrow \mu_{\text{eff}} = \rho_{\text{eff}} \left[ \alpha \left( \frac{Z_{\text{eff}}^d}{E^g} \right) + \beta f_{KN}(E) \right] \end{aligned} \quad (8)$$

where  $\alpha$  and  $\beta$  are constants,  $d \approx 3 - 4$ ,  $g \approx 3 - 3.5$  and  $f_{KN}(E)$  is the Klein–Nishina function. The right term of the third part of Eq. 8 is the linear combination, respectively, of the photoelectric [ $\alpha(Z_{\text{eff}}^d/E^g)$ ] and Compton [ $\beta f_{KN}(E)$ ] interactions. Conversely, after obtaining two measurements of attenuation coefficient with two different X-ray energies, any material can be characterized in terms of  $\rho_{\text{eff}}$  and  $Z_{\text{eff}}$ . The work of Alvarez and Macovski is at the basis of the Rho-Z ( $\rho Z$ ) algorithms for material decomposition and the

two-basis-material decomposition in the projection domain (raw data) (Fig. 3) [2, 3].

Starting from the work of Alvarez and Macovski, Kalender et al. defined the mass attenuation coefficient of a given mixture, as function of energy [ $(\mu/\rho)(E)$ ], with a linear combination of the mass attenuation coefficients of two hypothetical known basis materials (1 and 2) present at different mass densities ( $\rho_1$  and  $\rho_2$ , see also the weight fractions  $w_i$  in Eq. 6) at the spatial location  $r$ :

$$\mu(r, E) = \rho_1(r) \cdot \left( \frac{\mu}{\rho} \right)_1(E) + \rho_2(r) \cdot \left( \frac{\mu}{\rho} \right)_2(E) \quad (9)$$

The linear attenuation coefficient at a given spatial location  $\mu(r, E)$  (i.e., the measured attenuation in CT) is the sum of two known materials with known mass attenuation coefficients [ $(\mu/\rho)_{1,2}$ ] present at unknown mass densities within the voxel (unknown  $\rho_{1,2}$ ); the equation has no solution when a single X-ray spectrum is used [13].

If we measure the attenuation coefficients after irradiation with two X-ray energies (high and low,  $H$  and  $L$ ,  $I_H$  and  $I_L$ ), Eq. 9 can be solved as a system of two equations with two solutions ( $(\mu(r, E)_{H, 1})$  and two unknowns ( $\rho_{1,2}$ ). This concept transferred to CT imaging with polychromatic X-ray beams by the implementation of the line integral over the linear attenuation coefficient for each X-ray projection, and by the definition of the area densities ( $\delta_{1,2}$ ), which are calculated from the unknowns  $\rho_{1,2}$  (see Eqs. 3, 5 and 9):

$$\begin{cases} \mu(r, E)_H = \rho_1(r) \cdot \left( \frac{\mu}{\rho} \right)_1(E) + \rho_2(r) \cdot \left( \frac{\mu}{\rho} \right)_2(E) \\ \mu(r, E)_L = \rho_1(r) \cdot \left( \frac{\mu}{\rho} \right)_1(E) + \rho_2(r) \cdot \left( \frac{\mu}{\rho} \right)_2(E) \end{cases} \Rightarrow \begin{cases} I_H = \int I_{0,H}(E) \cdot e^{[-\delta_1 \left( \frac{\mu}{\rho} \right)_1(E) - \delta_2 \left( \frac{\mu}{\rho} \right)_2(E)]} dE \\ I_L = \int I_{0,L}(E) \cdot e^{[-\delta_1 \left( \frac{\mu}{\rho} \right)_1(E) - \delta_2 \left( \frac{\mu}{\rho} \right)_2(E)]} dE \end{cases} \quad (10)$$

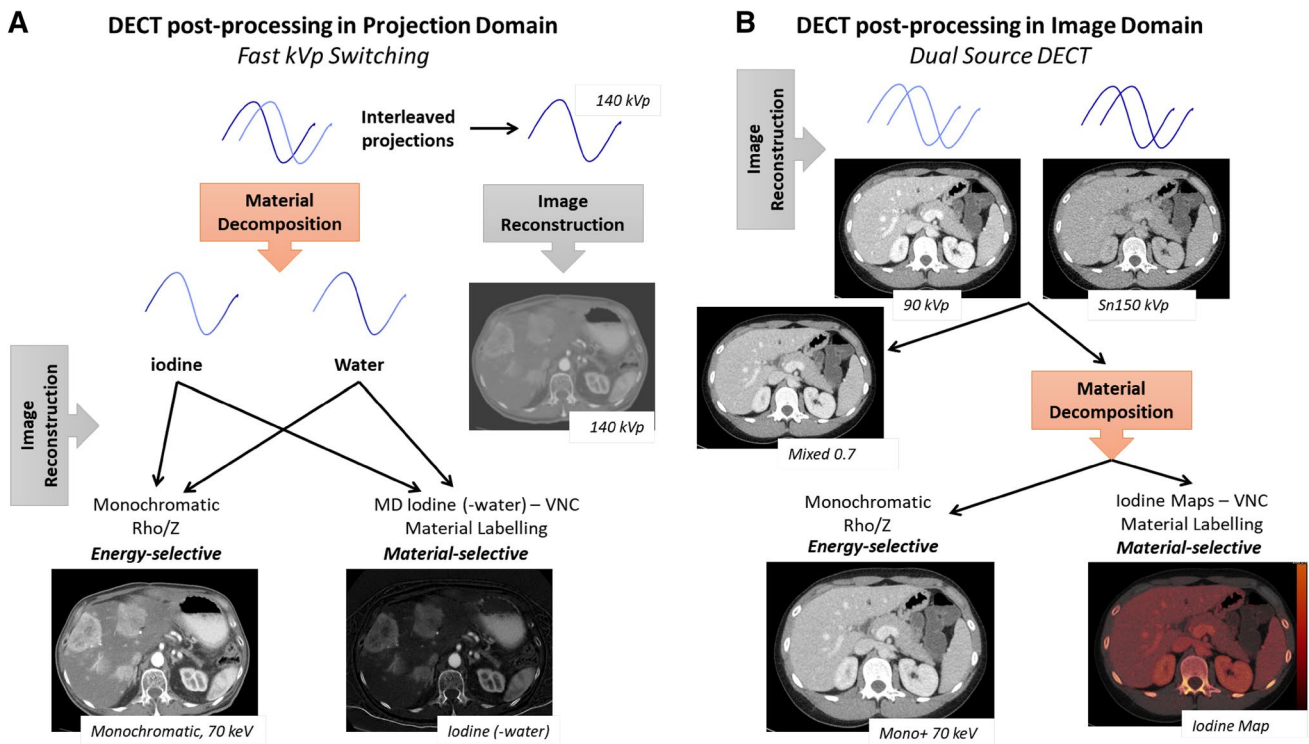


**Fig. 3** Processing and reconstruction of dual-energy datasets. **a** Example of material decomposition in projection domain in the fast kVp switching scanner. The material decomposition is performed on the projections to obtain information on basis materials. These data are used to reconstruct energy-selective and material-selective images. The scanner also provides a 140-kVp image from the respec-

tive projections. **b** Example of material decomposition in image domain in the dual-source scanner. The two datasets (high energy and low energy) are reconstructed and are used for material decomposition (energy- and material-selective images, as well as for producing mixed images (where the CT numbers in each pixel are a weighted sum of the corresponding CT numbers in the two datasets))

with

$$\delta_i = \int \rho_i(r) dx. \tag{11}$$

The application of this algorithm allows for obtaining material-selective images, where the basis materials (e.g., calcium and iodine) are detected, labeled, quantified, displayed or subtracted (e.g., the iodine maps or the virtual non-contrast images) (Fig. 3) [13].

After calculation of the effective densities of the basis materials ( $\rho_1$  and  $\rho_2$ ), the linear attenuation coefficient of the mixture  $\mu(r, E)$ , thus the CT numbers, can be calculated by simulating the irradiation with a virtual monochromatic beam in a wide range of energies even out of the energy range effectively used. These images are called virtual monoenergetic images (VMI) (Fig. 3). VMI at low keV are useful for highlighting focal lesions in condition of low contrast (e.g., in liver or pancreas) (Fig. 4) or for improvement of the contrast-to-noise ratio and reduction of the administered contrast material [14]. Conversely, VMI at high keV are useful for reduction of proton-starving and beam-hardening artifacts in the presence of metallic objects at the expense of contrast (Fig. 5) [15]. A drawback of some

VMI algorithms is the increasing noise at lower energies; this problem has been addressed with the introduction of noise-corrected VMI (MonoPlus, Monoenergetic Plus, Siemens Healthineers) [16]. The theoretical advantage of the approach in the projection domain is the avoidance of beam-hardening artifacts: the linear attenuation coefficient is obtained from the attenuation coefficient of the basis materials at the calculated mass densities [13].

A critical issue of the projection domain approach is the large amount of data processed and the high computational power required: the post-processing of dual-energy data could be easier on reconstructed images (Fig. 3) [13]. Equation 8 can be defined as the linear combination of the mass attenuation coefficients of two basis materials present in the mixture with fractional masses of  $m_1 + m_2 = 1$  (being  $m_2 = 1 - m_1$ ). Also, the effective linear attenuation coefficient ( $\mu_{\text{eff}}$ ) can be calculated from the CT numbers (CT#) as in Eq. 4:

$$\begin{aligned} \mu_{\text{eff}} &= \left( \frac{\text{CT\#}}{1000} + 1 \right) \mu_{\text{water}} = \rho_{\text{eff}} \left[ \alpha \left( \frac{Z_{\text{eff}}^d}{E_s} \right) + \beta f_{KN}(E) \right] \\ &= \rho_{\text{eff}} \left[ m_1 \left( \frac{\mu}{\rho} \right)_1 + (1 - m_1) \left( \frac{\mu}{\rho} \right)_2 \right]. \end{aligned} \tag{12}$$

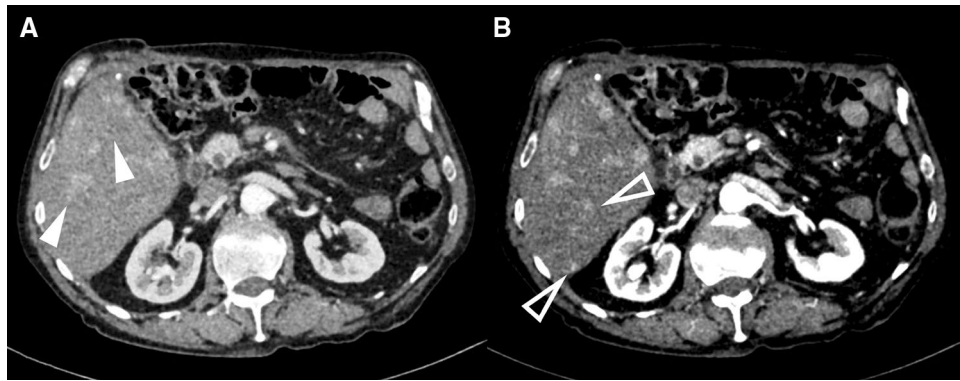
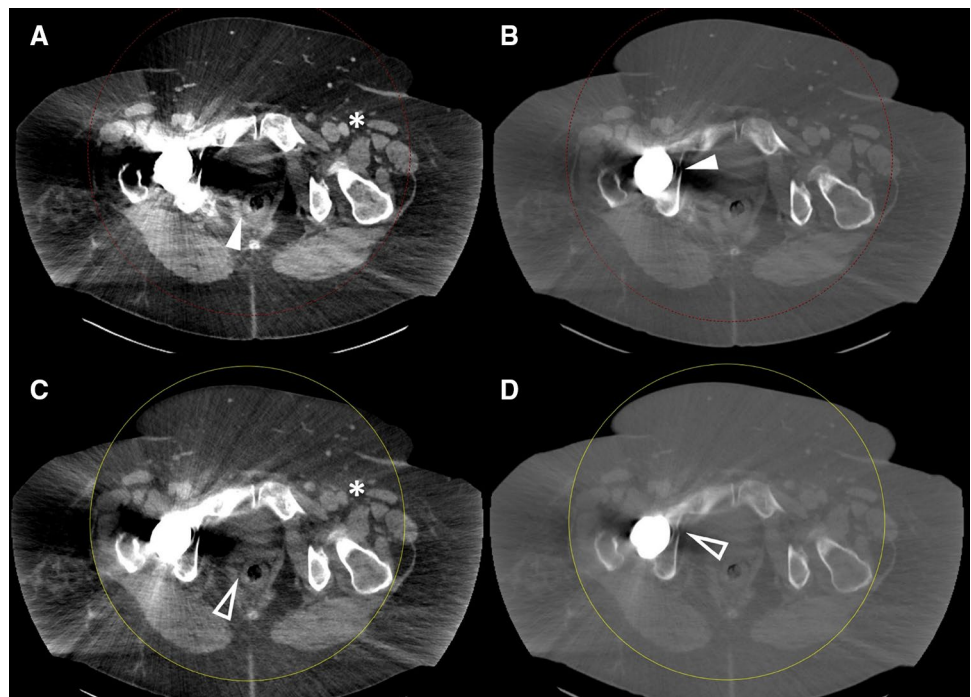


**Fig. 4** Male, 70 y.o., follow-up for neuroendocrine tumor. Third-generation dual-source CT (Somatom Force, Siemens Healthineers). **a** Dual-energy acquisition, 80/150 kVp, mixed 0.8, arterial phase; arrowheads: liver metastases. **b** Monoenergetic Plus (MonoPlus, Sie-

mens Healthineers), 55 keV. Despite the strong weighting of the low voltage on image a, the monoenergetic plus reconstruction allows for better visualization of a higher number of liver metastases (empty arrowheads)

**Fig. 5** Female, 68 y.o., right hip prosthesis. Third-generation dual-source CT (Somatom Force, Siemens Healthineers). **a, b** Dual-energy acquisitions 100/150 kVp, mixed 0.8, venous phase, soft-tissue window (**a**) and bone window (**b**). Marked beam-hardening and photon-starving artifacts are present close to the prosthesis (arrowheads) limiting the evaluation of the soft tissues (**a**) and the cortical bone (**b**). \*: left femoral vessels. **c, d** Monoenergetic Plus reconstructions (MonoPlus, Siemens Healthineers), 130 keV, soft tissue (**c**) and bone (**d**) window. The artifacts are reduced, the visualization of pelvic soft tissues (**c**) and the cortical bone (**d**) are improved (empty arrowheads) at the expense of contrast (\*)



The effective linear attenuation coefficient is calculated from the CT number (CT#), it is a function of photoelectric and Compton interaction of a mixture with an atomic number  $Z_{\text{eff}}$  but can also be defined as a function of two unknowns: the effective mass density ( $\rho_{\text{eff}}$ ) and the fractional mass of one basis material ( $m_1$ ). The CT acquisition with two different X-ray energy spectra ( $H$  and  $L$ ) provides two datasets of reconstructed images that can be processed to obtain the two unknowns:

$$\begin{cases} \left( \frac{\text{CT}_{\#H}}{1000} + 1 \right) \mu_{\text{water}} = \rho_{\text{eff}} \left[ m_1 \left( \frac{\mu}{\rho} \right)_{1,H} + (1 - m_1) \left( \frac{\mu}{\rho} \right)_{2,H} \right] \\ \left( \frac{\text{CT}_{\#L}}{1000} + 1 \right) \mu_{\text{water}} = \rho_{\text{eff}} \left[ m_1 \left( \frac{\mu}{\rho} \right)_{1,L} + (1 - m_1) \left( \frac{\mu}{\rho} \right)_{2,L} \right] \end{cases} \quad (13)$$

This is the concept behind the material decomposition on image domain. In this case, since the reconstructed images are used, the beam-hardening artifacts are not automatically removed and need to be corrected [17]. Maas et al. proposed a hybrid algorithm with a pre-processing in the projection domain to reduce beam-hardening artifacts [18].

An interesting point is that any material with different atomic number than the chosen basis material variably contributes (and is characterized as) to the attenuation of each of the basis material in all of these algorithms [13]. Theoretically, the more the basis materials are included, the more accurate it is in quantification of basis materials. A classical case was the calcium quantification in osteoporosis with dual-energy acquisitions of vertebral bones, with a mixture of calcium, fat (yellow marrow) and water or soft tissue (red marrow). A two-basis-material decomposition algorithm will not be accurate enough for calcium estimation due to the significant differences in attenuation of soft tissue and fat. A three-basis-material decomposition algorithm would be a more accurate model. The easier way comes from Goodsitt et al. [19]. The authors started from the hypothesis that the effective linear attenuation coefficient in function of X-ray energy  $\mu_{\text{eff}}(E)$  comes from the sum of the mass attenuation coefficients of each basis material ( $i$ ) multiplied by their concentrations (the concentration  $c_i$  is defined as the product between the fractional volume  $V_i$  and mass density  $\rho_i$ ), similarly to what expressed in Eqs. 6, 9, 10, 12, and 13:

$$\mu_{\text{eff}}(E) = \sum_i \left( \frac{\mu_i(E)}{\rho_i} \right) c_i \tag{14}$$

If the linear attenuation coefficients in Eq. 14 are substituted as in Eq. 4 and the conservation of volumes is respected, a system of three equations in three unknowns (fractional volumes  $V_i$ ) can be solved after CT acquisition at two energies ( $H, L$ ):

$$\begin{cases} \text{CT}(H) = V_1\text{CT}\#_1(H) + V_2\text{CT}\#_2(H) + V_3\text{CT}\#_3(H) \\ \text{CT}(L) = V_1\text{CT}\#_1(L) + V_2\text{CT}\#_2(L) + V_3\text{CT}\#_3(L) \\ V_1 + V_2 + V_3 = 1 \end{cases} \tag{15}$$

where  $\text{CT}\#_i(E)$  are the CT numbers of pure basis materials at the given X-ray energy, previously obtained (e.g., calcium hydroxyapatite as a model for bone). This model allows for calculation, in the image domain, of relative quantities (fractional volumes) of three basis materials, by two measurements (acquisitions at two different energies) with a third condition (the conservation of volume). The model cannot be generalized because the conservation of volume is not always respected (e.g., salt in water or iron in fat or soft tissue).

A more generalized model was proposed by Liu et al. [20], based on conservation of mass. In the first step of the model, the dual-energy datasets are used to calculate the  $\rho_{\text{eff}}$  and  $Z_{\text{eff}}$ . In the second step, the  $\rho_{\text{eff}}$  is used in a system of three equations where the fractional masses of the three materials are the unknowns and the conservation of mass is respected:

$$\begin{cases} \mu_{\text{eff},L} = \rho_{\text{eff}} \int \left[ m_1 \left( \frac{\mu}{\rho} \right)_1(E) + m_2 \left( \frac{\mu}{\rho} \right)_2(E) + m_3 \left( \frac{\mu}{\rho} \right)_3(E) \right] dE \\ \mu_{\text{eff},H} = \rho_{\text{eff}} \int \left[ m_1 \left( \frac{\mu}{\rho} \right)_1(E) + m_2 \left( \frac{\mu}{\rho} \right)_2(E) + m_3 \left( \frac{\mu}{\rho} \right)_3(E) \right] dE \\ m_1 + m_2 + m_3 = 1 \end{cases} \tag{16}$$

This is the concept behind the three-basis-material (or multimaterial) decomposition algorithms. Nowadays, the material decomposition and labeling algorithms on the different scanners may use algorithms with graphic vectors

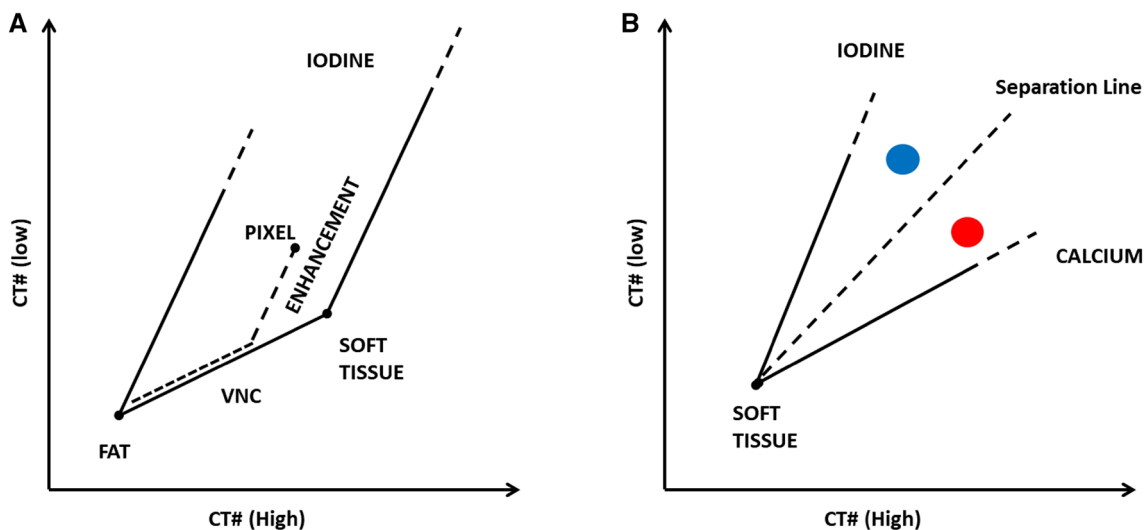


**Fig. 6** Three-basis-material decomposition (a) and labeling (b) with vectorial methods. In a, the dashed line is used for the evaluation of contrast enhancement (i.e., iodine quantification on iodine maps). In

b, the blue dot over the separation line is the pixel labeled as iodine, while the red dot is the pixel labeled as calcium (see also Fig. 2)

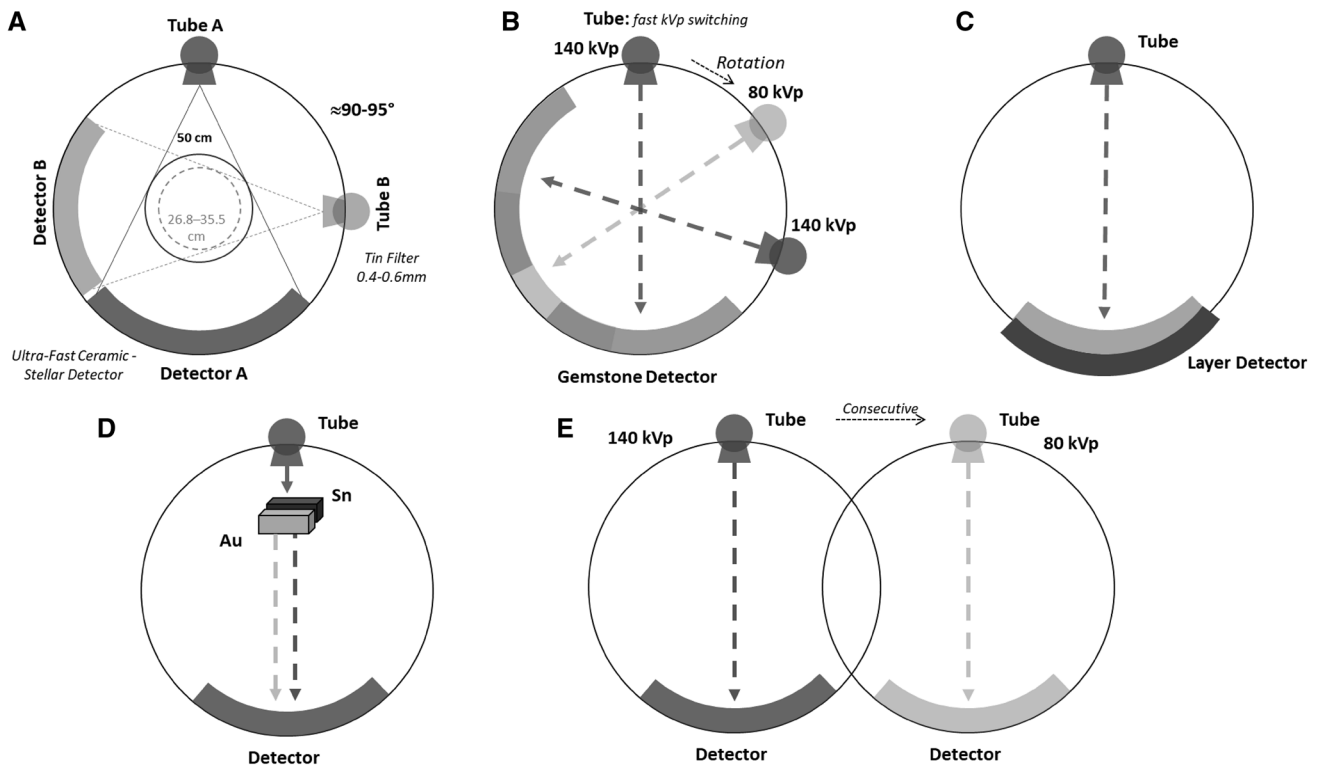


**Fig. 7** DECT scanner design. **a** Dual source: two tubes working at different voltages and two asymmetrical detectors are mounted with an offset of nearly  $90^\circ$ , increased in the latest generation to improve the FOV of system B up to 35.5 cm. The tin filtration for better spectral separation is possible with these scanners. **b** Fast kVp switching. The X-ray tube switches between 80 kVp and 140 kVp while rotating, allowing for the acquisition of DECT datasets. The Gemstone detec-

tor allows for a rapid response. **c** Layer detector. The detector is composed of two layers sensitive to different energy levels of the incident beam; the spectral separation is performed only by the detector. **d** Split filter. A filter composed of tin and gold filtrates, respectively, the lower and higher parts of the X-ray spectrum, thus splitting the X-ray beam. **e** Consecutive acquisitions: two consecutive acquisitions, spiral or sequential, at two different energy levels, are performed

based on equations described in this section (Fig. 6) [21, 22].

## Dual-energy CT: the technology

Five different technologies are available for acquisition of DECT datasets: dual-source, fast kVp switching, layer detector, twin beam and consecutive scans (Fig. 7).

### Dual-source dual-energy CT (dsDECT)

The dsDECT was the first technology introduced in clinical routine since 2006 by Siemens Healthineers (Forchheim, Germany) with the three generations of Somatom scanners (Definition [1st], Flash [2nd], and Force [3rd]). The scanners have two independent X-ray tubes coupled with two independent detectors; each set is mounted within the gantry with an offset of  $\sim 90^\circ$ . The main purpose of this architecture was of achieving a temporal resolution acceptable for cardiac studies ( $< 100$  ms: 65–85 ms) with both

tubes working (Flash or TurboFlash acquisition, Siemens Healthineers); the dual-energy mode with the two tubes at different kVp is a natural corollary in these scanners [4, 23].

Due to engineering issues (balance and space in the gantry), the two detectors are asymmetrical with the smaller detector B limited to a field of view (FOV) of 266 mm in the first generation (thus limiting the FOV for material decomposition). This drawback was improved in the second and third generations by increasing the offset and allowing for bigger detector B (FOV up to 355 mm in Force) (Fig. 7).

A second important point is the tube technology. The Straton tube in the first generation was capable of 20 kV steps between 80 and 140 kV in the first generation, allowing for the combination of 80/140 kV in dual-energy acquisitions. In the second generation, a tin filter (0.4 mm) was added to improve the spectral separation (the robustness of material decomposition algorithms is proportional to separation of the two X-ray spectra) allowing for two combinations in dual-energy acquisitions (80/140 kV; 100/140 Sn kV) [24]. In the third generation, the Vectron tube was introduced: it is capable of 10 kV steps between 70 kV and



150 kV with a maximum current of 1300 mA at 70 kV. This technology allows for (1) a more frequent use of low voltages (contrast and dose reduction) and (2) better spectral separation (70–100 kV/140–150 Sn kV). Moreover, the higher power allows for a more aggressive filtration at high voltages (0.6 mm tin) with further improvement of spectral separation (Fig. 7) [25].

With the newer generations, the rotation speed was improved (up to 0.25s) with no limitations for dual energy, together with the Z-axis coverage and the introduction of integrated Stellar detectors (the lower noise in the stellar detectors improved the material decomposition). Iterative reconstructions can be used with both tubes [25].

This technical solution requires the material decomposition to be performed on image domain (due to  $\sim 90^\circ$  offset of the projections), and adequate algorithms are implemented to reduce the cross-scattered radiation between the two systems. Besides the material decomposition, virtual monochromatic and Rho-Z methods, the scanner provides the blended (mixed) images for reading and reporting, in which the pixels are a weighted sum of the CT numbers from the high- and low-energy datasets, without any material decomposition performed (Fig. 3) [23].

### Fast kVp switching

In the fast kVp switching scanners (Discovery CT 750 HD and Revolution, GE Healthcare, Milwaukee, WI), the X-ray tube switches between 80 and 140 kVp in less than 0.2 ms, thus acquiring high- and low-energy projections within the same rotation with almost no-temporal mismatch and at a full FOV of 50 cm.

Regarding the X-ray tube, the spectral separation (and the material decomposition) is affected by the ramp-up and ramp-down of the tube voltages while switching. At low voltage, the photon output is lower and the noise increases: higher current and longer exposure time are necessary at low kV (typical exposure ratio: 80/140 kVp = 60%/40%); the automatic current modulation is not feasible in this configuration, and the dose reduction is implemented only with the iterative reconstructions. A too fast rotation speed reduces the number of projections acquired with poor quality of datasets; the rotation time is limited to 0.5s.

A detector with adequate response is also necessary: the Gemstone Clarity detector (GE Healthcare, Milwaukee WI) has a primary decay faster than and an afterglow significantly lower than Gd-based scintillators (Fig. 7).

The small offset between the projections at high and low energies ( $< 0.5^\circ$ ) allows for material decomposition in projection domain (Fig. 3) [26].

### Dual-layer detectors

In the iQon Spectral (Philips Healthcare, The Netherlands) the tube gives a polychromatic X-ray beam (120 or 140 kVp), and the spectral separation is performed by the layer detector and not by the tube.

The layer detector is composed of two layers: the inner one, with ZnSe crystals, is sensitive to low energies, while the external one (with GdOS detectors) is sensitive to the higher energy of the spectrum (Fig. 7). A challenge for the detector is the presence of high-attenuation objects reducing the lower component of the spectrum for the internal layer. The remnant X-ray beam arriving at the external layer results from a strong filtration of internal layer. Other challenges in detector design are the position of the photodiodes and the necessary presence of an antiscatter grid reducing the optical sensitivity when compared to conventional detectors with photodiodes below the scintillator. Moreover, scattering may cause cross talk between layers.

The dual-energy datasets are acquired at a full FOV with no limits in rotation speed. The material decomposition is performed in the projection domain thanks to the null offset of the projections (Fig. 3). Conventional CT images are reconstructed by weighted summation of the high- and low-energy datasets; iterative reconstructions can be used for dose reduction [22].

### The split filter

The split filter in the Somatom Edge TwinBeam (Siemens Healthineers, Forchheim, Germany) is composed of two different metals: tin and gold, which, respectively, filter the low and high components to split a polychromatic X-ray beam. The dual-energy datasets are acquired with each half of the detector receiving the split beam. This allows for dual-energy information at full FOV of 50 cm with no limitations in rotation speed. Potential drawbacks are the short pitch values (0.3–0.5), the necessary high power of the tube because of filtration, with potential limitations in larger patients, and the limited spectral separation (Fig. 7) [27].

### Consecutive acquisitions

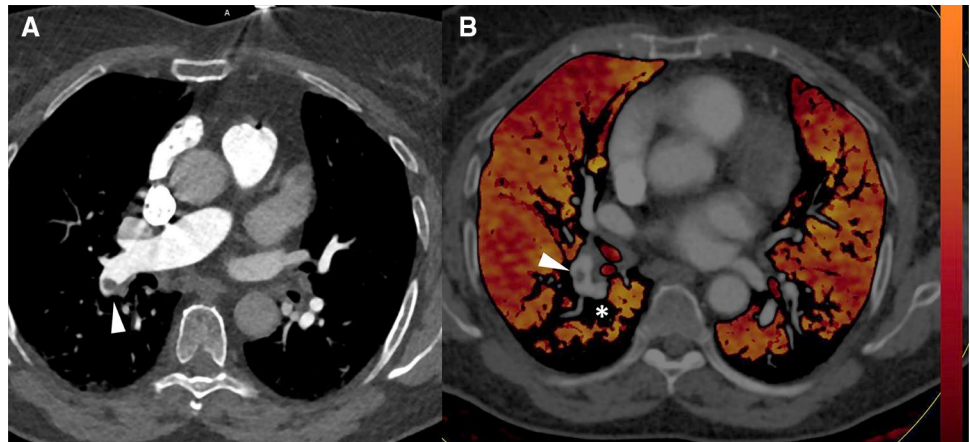
This method does not require a dedicated hardware. However, the low temporal resolution and related motion artifacts limit the application to non-contrast studies or to anatomical districts without significant movements. Dose reduction techniques, such as automatic current modulation, can be used (Fig. 7) [28].

**Table 1** Post-processing of DECT datasets: algorithms, concepts and examples of clinical applications

Algorithm	Concept	Examples of clinical applications
Material decomposition	Material labeling	<ul style="list-style-type: none"> <li>• Contrast enhancement and hemorrhagic lesions (iodine vs. iron) [29];</li> <li>• Plaque characterization: calcium, fibrous, necrotic and lipidic components [37];</li> <li>• Urinary stone composition (urate vs. non-urate) [52];</li> <li>• Crystal characterization in arthropathies (urate and gout) [54, 55];</li> <li>• Hemosiderin deposits in villonodular synovitis (iron) [54, 55].</li> </ul>
	Material quantification	<ul style="list-style-type: none"> <li>• Pulmonary embolism and perfusion (iodine) [30, 31];</li> <li>• Lung perfusion (xenon, crypton) [32, 33];</li> <li>• Myocardial perfusion (iodine) [34];</li> <li>• Lesion contrast enhancement: solid versus cystic (iodine) [45];</li> <li>• Lesion characterization (iodine) [46];</li> <li>• Tumor treatment response to therapy: necrosis or changes in iodine uptake [47–49];</li> <li>• Evaluation of inflammatory, vascular and neoplastic lesions in gastrointestinal tract (iodine) [50];</li> <li>• Surrogate of perfusion parameters (iodine) [51];</li> <li>• Iron quantification in liver [53].</li> </ul>
	Material subtraction	<ul style="list-style-type: none"> <li>• VNC: Iodine subtraction and dose reduction by avoiding basal acquisition (abdominal, vascular and musculoskeletal studies) [38–42, 59, 60];</li> <li>• Calcium score: selective subtraction of Iodine maintaining coronary calcium [34–36];</li> <li>• Bone removal for vascular studies (calcium) [36];</li> <li>• Plaque subtraction (calcium) and evaluation of vascular lumen [35, 36];</li> <li>• Virtual non-calcium: evaluation of bone edema [57, 58].</li> </ul>
Energy-selective images	Virtual monochromatic images	<ul style="list-style-type: none"> <li>• Reduction of dose of contrast material: pulmonary embolism and cardiovascular studies [14, 64–66];</li> <li>• Improved contrast in selected structured (abdominal) [61–63];</li> <li>• Artifact reductions: metal prostheses [15].</li> </ul>
Rho-Z methods and spectral curve	Evaluation of effective density and effective atomic (electron) number of the scanned mixture with unknown spectral properties	<ul style="list-style-type: none"> <li>• Non-calcific gallstones [69];</li> <li>• Evaluation of cartilages and tendons [59];</li> <li>• Detection and characterization of foreign bodies [68].</li> </ul>

Table showing a classification of algorithms available for post-processing of DECT datasets. The concept behind each class of algorithms is explained, and some examples of clinical applications are reported. DECT: dual-energy CT, VNC: virtual non-contrast

**Fig. 8** Female, 82 y.o., pulmonary embolism scanned with a dual-source CT (Somatom Force, Siemens Healthineers). **a** CT angiography of pulmonary artery showing an embolus on the right (arrowhead); high-pitch, TurboFlash mode (Siemens Healthineers), 80 kVp. **b** Iodine map (red) showing a perfusion defect (\*) in the right lower lobe close to the pulmonary embolus (arrowhead); dual-energy acquisition 90/150 Sn, iodine overlay—CT



### Dual-energy CT: post-processing and clinical applications

The applications of dual-energy can be divided in material-selective and energy-selective. The former includes material decomposition with material labeling, quantification (distribution maps) and subtraction (VNC); the latter includes the monoenergetic imaging, effective atomic number and effective electron density (Rho-Z maps). Table 1 provides an overview of the algorithms and main clinical application dual-energy techniques.

#### Material-selective images: material subtraction, quantification and labeling

With material-selective images, a given basis material is detected, labeled and subtracted: iodine, calcium or other known materials (e.g., monosodium urate) are frequently used as basis material.

In neuroradiology, the main application of material decomposition is the material labeling and quantification of iodine in the presence of hemorrhagic material. The evaluation of contrast enhancement of a hemorrhagic brain lesion may be challenging in both CT and in magnetic resonance (MRI), while DECT is able to distinguish the different spectral characteristics of iodine and iron. Kim et al. [29] demonstrated a significantly higher sensitivity of iodine maps fused with virtual unenhanced images for detection of enhancing hemorrhagic brain lesions.

In thoracic imaging, iodine maps allow for the evaluation of perfusion defects in pulmonary embolism, beyond the CT angiography, in acute and chronic setting (Fig. 8) [30, 31]. Gases with high atomic number, such as xenon or krypton, have been used for the evaluation of lung ventilation. Promising results have been recorded both with single-phase acquisitions and with dynamic studies [32, 33].

In cardiovascular imaging, the iodine maps are useful for the evaluation of myocardial perfusion while the selective

subtraction of iodine in virtual non-contrast (VNC) images provided good results for the calcium score [34–36]. Calcium labeling and subtraction with dual energy is useful for bone removal and plaque removal, improving the evaluation of vascular studies and the evaluation of vascular lumen [35, 36]. An interesting application of material decomposition is the characterization of the atherosclerotic plaque. Obaid et al. recorded an improved diagnostic accuracy with DECT in characterization lipidic, necrotic, fibrous components and calcium in atherosclerotic plaques [37].

An application of material decomposition in abdominal and oncological studies is the VNC reconstructions with avoidance of basal acquisitions and dose reduction, particularly relevant in selected populations (e.g., pediatric population) [38–42]. It has to be pointed that small, often unimportant, differences in attenuation values need to be accounted when using virtual non-contrast images in abdomen (Fig. 9) [43, 44]. The role of iodine maps is qualitative and quantitative. The evaluation of iodine maps allows for accurate discrimination between enhancing and unenhancing lesions: this may be relevant in complicated cystic lesions of the kidney [45]. The quantitative evaluation of iodine maps may be helpful for lesion characterization: Lv et al. [46] found significant differences in iodine uptake between hepatic hemangioma and hepatocellular carcinoma. Regarding treatment response, the iodine quantification showed promising results: changes in iodine uptake are a more accurate indicator of treatment response to target or antiangiogenic agents than morphological criteria [47–49]. The evaluation of iodine maps has demonstrated their utility in the evaluation of the gastrointestinal tract, improving the detection of inflammatory, vascular (ischemic) and neoplastic lesions [50]. Skornitzke et al. [51] tried to investigate the role of iodine uptake as surrogate of perfusion parameters, but the results are still under debate. Material labeling has been successfully implemented for the evaluation of urinary stone composition or for the labeling of iodine and calcium (Fig. 2) [52].

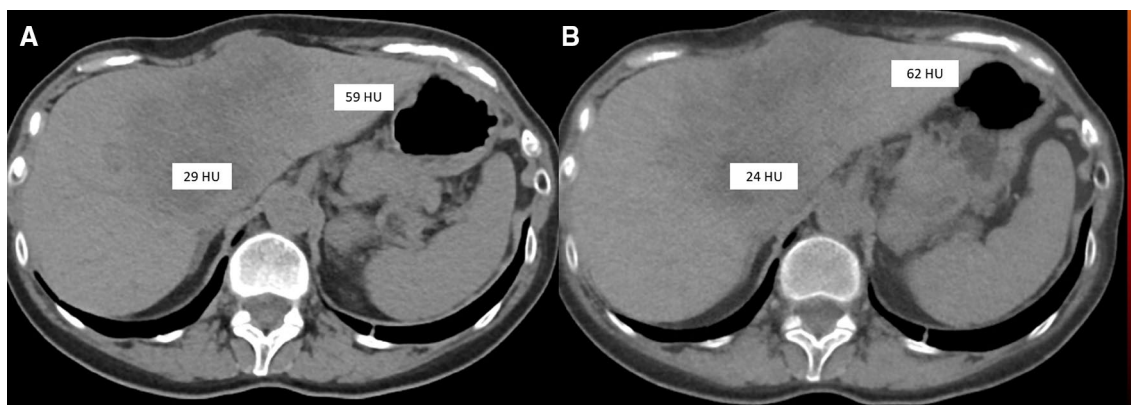


**Fig. 9** Female, 62 y.o., cholangiocellular carcinoma. Third-generation dual-source CT (Somatom Force, Siemens Healthineers). **a** Basal scan, 120 kVp. **b** Dual-energy acquisition, venous phase (90–150 Sn kVp), 3-basis-material decomposition (Liver VNC, Siemens Health-

ineers), virtual non-contrast. Virtual non-contrast acquisitions are of good quality, may be useful for avoiding basal acquisitions, but sometimes present variable differences in attenuation when compared to basal acquisitions

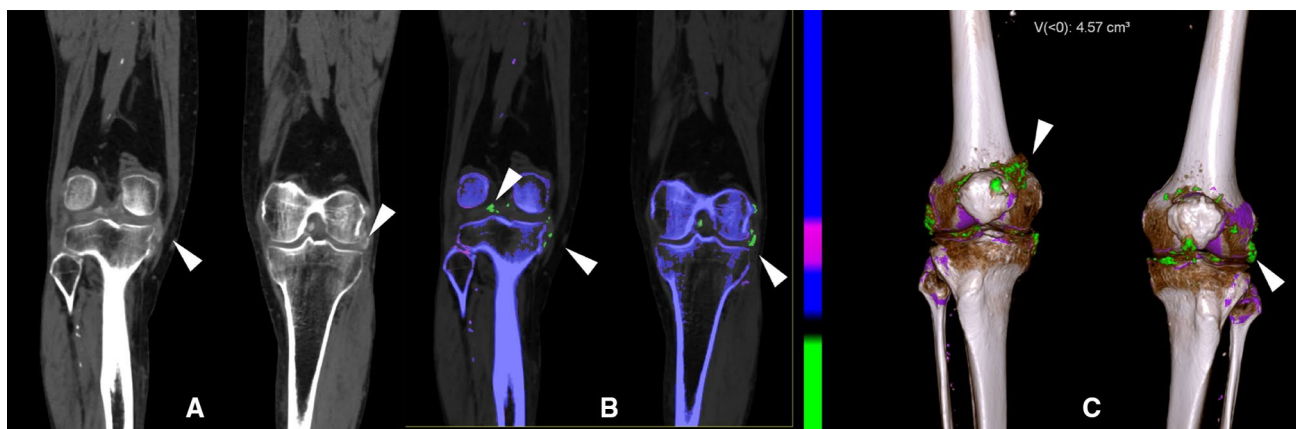


**Fig. 10** Third-generation dual-source CT (Somatom Force, Siemens Healthineers). Male, 73 y.o., gout. **a** Dual-energy acquisition, 80/150 Sn kVp, mixed 0.5, coronal; arrowheads on hyperdense deposits on the right and left knees. Material decomposition allows

for labeling of monosodium urate crystals in green on coronal (**b**) and volume rendering (VR) reconstructions (**c**) (arrowheads) with volumetric estimation

In liver imaging, the iron quantification with DECT is an important tool when MRI is contraindicated [53].

In musculoskeletal radiology, material labeling is useful for the quantification of monosodium urate crystals in gout and differentiation with other crystal arthropathies (Fig. 10) [54, 55]. Moreover, DECT allows for demonstration of hemosiderin deposits in pigmented villonodular synovitis [56]. The evaluation of bone marrow disorders, typically evaluated with MRI, is an expanding application of material decomposition: DECT is useful for depiction of bone marrow edema and bone lesions (three-material decomposition and virtual non-calcium) [57, 58]. VNC and iodine subtraction are also useful in the case of intravenous contrast injection or in CT arthrography [59, 60].

### Energy-selective applications: virtual monoenergetic images and Rho-Z methods

VMI are produced with the linear attenuation coefficients of basis materials obtained from the material decomposition, with the possibility of reconstruction of simulated images in a wide range of energy levels, within or out of the ranges effectively used. The utility in clinical practice relies in the use of a monochromatic beam close to the k-edge of a basis material (e.g., iodine) resulting in improved visualization of that given material (e.g., better contrast). Conversely, the use of a virtual monochromatic beam far for the attenuation edge of a given material may be helpful for reduction of proton-starving and beam-hardening artifacts [15, 61].

VMI at low keV improves the detection of low-enhancing lesions, particularly in organs with relatively poor contrast

(Fig. 4). The VMI reconstructions have demonstrated promising results for the evaluation of pancreatic adenocarcinomas, focal liver lesions (Fig. 4) or for the extension of endometrial adenocarcinomas [61–63]. Another field of applications is the optimization of contrast, similarly to acquisitions at low voltages (not always possible), with potential reduction of the dose of contrast material, in particular in cardiovascular imaging, and in the evaluation of pulmonary embolism [14, 64–66]. VMI at high keV simulate the use of high-energy X-ray beams and are useful for attenuation of beam-hardening artifacts at the expense of contrast (Fig. 5) [15].

A material or a mixture with unknown attenuation coefficients can be semiquantitatively assessed on the spectral curve and highlighted; this is the case of biliary non-calcific stones or foreign bodies, such as in drug mules [67–69].

Finally, the Rho-Z methods still have more limited implementation: interesting applications in tissue characterization, mainly in cartilages and tendons [59].

## Conclusion

In this review, we have provided a brief overview on physical and theoretical principles, and clinical applications of dual-energy CT, which is a growing technique with expanding applications.

**Funding** No funding was received for this paper.

## Compliance with ethical standards

**Conflict of interest** AA is a speaker for Siemens Healthineers. The other authors have no conflict of interest to declare.

## References

- Hounsfield GN (1973) Computerized transverse axial scanning (tomography): Part 1. Description of system. *Br J Radiol* 46:1016–1022
- Alvarez RE, Macovski A (1976) Energy-selective reconstructions in X-ray computerized tomography. *Phys Med Biol* 21:733–744
- Macovski A, Alvarez RE, Chan JL, Stonestrom JP, Zatz LM (1976) Energy dependent reconstruction in X-ray computerized tomography. *Comput Biol Med* 6:325–336
- Flohr TG, McCollough CH, Bruder H et al (2006) First performance evaluation of a dual-source CT (DSCT) system. *Eur Radiol* 16:256–268
- Bushberg JT (1998) The AAPM/RSNA physics tutorial for residents. X-ray interactions. *RadioGraphics* 18:457–468
- Buzug TM (2008) Fundamentals of X-rays Physics. In: Buzug TM (ed) *Computed tomography from photon statistics to modern cone-beam CT*. Springer, Berlin, pp 14–73
- Chandra R, Rahmin A (2018) Interaction of high-energy radiation with matter. In: Chandra R, Rahmin A (eds) *Nuclear medicine physics. The basics*, 8th edn. Wolters Kluwer
- McCullough EC (1975) Photon attenuation in computed tomography. *Med Phys* 2:307–320
- Brooks RA, Di Chiro G (1976) Principles of computer assisted tomography (CAT) in radiographic and radioisotopic imaging. *Phys Med Biol* 21:689–732
- McCullough CH, Leng S, Yu L, Fletcher JG (2015) Dual- and multi-energy CT: principles, technical approaches, and clinical applications. *Radiology* 276:637–653
- Hubbell JH (1969) Photon cross sections, attenuation coefficients, and energy absorption coefficients from 10 keV to 100 GeV. National Bureau of Standards, Gaithersburg
- Hubbell JH (1977) Photon mass attenuation and mass energy-absorption coefficients for H, C, N, O, Ar, and seven mixtures from 0.1 keV to 20 MeV. *Radiat Res* 70:58–81
- Kalender WA, Perman WH, Vetter JR, Klotz E (1986) Evaluation of a prototype dual-energy computed tomographic apparatus. *I. Phantom Stud Med Phys* 13:334–339
- Zhao Y, Wu Y, Zuo Z, Cheng S (2017) CT angiography of the kidney using routine CT and the latest gemstone spectral Imaging combination of different noise indexes: image quality and radiation dose. *Radiol Med* 122:327–336
- Magarelli N, De Santis V, Marziali G et al (2018) Application and advantages of monoenergetic reconstruction images for the reduction of metallic artifacts using dual-energy CT in knee and hip prostheses. *Radiol Med* 123:593–600
- Grant KL, Flohr TG, Krauss B, Sedlmair M, Thomas C, Schmidt B (2014) Assessment of an advanced image-based technique to calculate virtual monoenergetic computed tomographic images from a dual-energy examination to improve contrast-to-noise ratio in examinations using iodinated contrast media. *Invest Radiol* 49:586–592
- McCullough CH, Schmidt B, Liu X, Yu L, Leng S (2011) Dual-energy algorithms and postprocessing techniques. In: Johnson TRC, Fink C, Schönberg SO, Reiser MF (eds) *Dual energy CT in clinical practice*. Springer, Berlin
- Maass C, Baer M, Kachelriess M (2009) Image-based dual energy CT using optimized precorrection functions: a practical new approach of material decomposition in image domain. *Med Phys* 36:3818–3829
- Goodsitt MM, Rosenthal DI, Reinus WR, Coumas J (1987) Two postprocessing CT techniques for determining the composition of trabecular bone. *Invest Radiol* 22:209–215
- Liu X, Yu L, Primak AN, McCollough CH (2009) Quantitative imaging of element composition and mass fraction using dual-energy CT: three-material decomposition. *Med Phys* 36:1602–1609
- Krauss B, Schmidt B, Flohr T (2011) Dual source CT. In: Johnson TRC, Fink C, Schönberg SO, Reiser MF (eds) *Dual energy CT in clinical practice*. Springer, Berlin
- Vlassenbroek A (2011) Dual layer CT. In: Johnson TRC, Fink C, Schönberg SO, Reiser MF (eds) *Dual energy CT in clinical practice*. Springer, Berlin
- Johnson TR, Krauss B, Sedlmair M et al (2007) Material differentiation by dual energy CT: initial experience. *Eur Radiol* 17:1510–1517
- Primak AN, Giraldo JC, Eusemann CD et al (2010) Dual-source dual-energy CT with additional tin filtration: dose and image quality evaluation in phantoms and in vivo. *AJR Am J Roentgenol* 195:1164–1174
- Krauss B, Grant KL, Schmidt BT, Flohr TG (2015) The importance of spectral separation: an assessment of dual-energy spectral separation for quantitative ability and dose efficiency. *Invest Radiol* 50:114–118

26. Zhang D, Li X, Liu B (2011) Objective characterization of GE discovery CT750 HD scanner: gemstone spectral imaging mode. *Med Phys* 38:1178–1188
27. Euler A, Parakh A, Falkowski AL et al (2016) Initial results of a single-source dual-energy computed tomography technique using a split-filter: assessment of image quality, radiation dose, and accuracy of dual-energy applications in an In Vitro and In Vivo study. *Invest Radiol*. <https://doi.org/10.1097/rli.0000000000000257>
28. Diekhoff T, Ziegeler K, Feist E et al (2015) First experience with single-source dual-energy computed tomography in six patients with acute arthralgia: a feasibility experiment using joint aspiration as a reference. *Skeletal Radiol* 44:1573–1577
29. Kim SJ, Lim HK, Lee HY et al (2012) Dual-energy CT in the evaluation of intracerebral hemorrhage of unknown origin: differentiation between tumor bleeding and pure hemorrhage. *AJNR Am J Neuroradiol* 33:865–872
30. Hong YJ, Kim JY, Choe KO et al (2013) Different perfusion pattern between acute and chronic pulmonary thromboembolism: evaluation with two-phase dual-energy perfusion CT. *AJR Am J Roentgenol* 200:812–817
31. Zhao Y, Zuo Z, Cheng S, Wu Y (2018) CT pulmonary angiography using organ dose modulation with an iterative reconstruction algorithm and 3D Smart mA in different body mass indices: image quality and radiation dose. *Radiol Med* 123:676–685
32. Hachulla AL, Pontana F, Wemeau-Stervinou L et al (2012) Krypton ventilation imaging using dual-energy CT in chronic obstructive pulmonary disease patients: initial experience. *Radiology* 263:253–259
33. Chae EJ, Seo JB, Goo HW et al (2008) Xenon ventilation CT with a dual-energy technique of dual-source CT: initial experience. *Radiology* 248:615–624
34. Jin KN, De Cecco CN, Caruso D et al (2016) Myocardial perfusion imaging with dual energy CT. *Eur J Radiol* 85:1914–1921
35. De Santis D, Jin KN, Schoepf UJ et al (2018) Heavily calcified coronary arteries: advanced calcium subtraction improves luminal visualization and diagnostic confidence in dual-energy coronary computed tomography angiography. *Invest Radiol* 53:103–109
36. Tran DN, Straka M, Roos JE, Napel S, Fleischmann D (2009) Dual-energy CT discrimination of iodine and calcium: experimental results and implications for lower extremity CT angiography. *Acad Radiol* 16:160–171
37. Obaid DR, Calvert PA, Gopalan D et al (2014) Dual-energy computed tomography imaging to determine atherosclerotic plaque composition: a prospective study with tissue validation. *J Cardiovasc Comput Tomogr* 8:230–237
38. Stagnaro N, Rizzo F, Torre M, Cittadini G, Magnano G (2017) Multimodality imaging of pediatric airways disease: indication and technique. *Radiol Med* 122:419–429
39. Toma P, Cannata V, Genovese E, Magistrelli A, Granata C (2017) Radiation exposure in diagnostic imaging: wisdom and prudence, but still a lot to understand. *Radiol Med* 122:215–220
40. Parakh A, Macri F, Sahani D (2018) Dual-energy computed tomography: dose reduction, series reduction, and contrast load reduction in dual-energy computed tomography. *Radiol Clin North Am* 56:601–624
41. Paolicchi F, Bastiani L, Guido D, Dore A, Aringhieri G, Caramella D (2018) Radiation dose exposure in patients affected by lymphoma undergoing repeat CT examinations: how to manage the radiation dose variability. *Radiol Med* 123:191–201
42. Agostini A, Mari A, Lanza C et al (2019) Trends in radiation dose and image quality for pediatric patients with a multidetector CT and a third-generation dual-source dual-energy CT. *Radiol Med* 124:745–752
43. De Cecco CN, Muscogiuri G, Schoepf UJ et al (2016) Virtual unenhanced imaging of the liver with third-generation dual-source dual-energy CT and advanced modeled iterative reconstruction. *Eur J Radiol* 85:1257–1264
44. Borhani AA, Kulzer M, Iranpour N et al (2017) Comparison of true unenhanced and virtual unenhanced (VUE) attenuation values in abdominopelvic single-source rapid kilovoltage-switching spectral CT. *Abdom Radiol NY* 42:710–717
45. Chandarana H, Megibow AJ, Cohen BA et al (2011) Iodine quantification with dual-energy CT: phantom study and preliminary experience with renal masses. *AJR Am J Roentgenol* 196:W693–700
46. Lv P, Lin XZ, Li J, Li W, Chen K (2011) Differentiation of small hepatic hemangioma from small hepatocellular carcinoma: recently introduced spectral CT method. *Radiology* 259:720–729
47. Dai X, Schlemmer H-P, Schmidt B et al (2013) Quantitative therapy response assessment by volumetric iodine-uptake measurement: initial experience in patients with advanced hepatocellular carcinoma treated with sorafenib. *Eur J Radiol* 82:327–334
48. Uhrig M, Sedlmair M, Schlemmer HP, Hassel JC, Ganten M (2013) Monitoring targeted therapy using dual-energy CT: semi-automatic RECIST plus supplementary functional information by quantifying iodine uptake of melanoma metastases. *Cancer Imaging* 13:306–313
49. Meyer M, Hohenberger P, Apfaltrer P et al (2013) CT-based response assessment of advanced gastrointestinal stromal tumor: dual energy CT provides a more predictive imaging biomarker of clinical benefit than RECIST or Choi criteria. *Eur J Radiol* 82:923–928
50. Fulwadhva UP, Wortman JR, Sodickson AD (2016) Use of dual-energy ct and iodine maps in evaluation of bowel disease. *RadioGraphics* 36:393–406
51. Skornitzke S, Kauczor H-U, Stiller W et al (2018) Dual-energy CT iodine maps as an alternative quantitative imaging biomarker to abdominal CT perfusion: determination of appropriate trigger delays for acquisition using bolus tracking. *Br J Radiol* 91:20170351
52. Leng S, Huang A, Cardona JM, Duan X, Williams JC, McCollough CH (2016) Dual-energy CT for quantification of urinary stone composition in mixed stones: a phantom study. *AJR Am J Roentgenol* 207:321–329
53. Luo XF, Xie XQ, Cheng S et al (2015) Dual-energy ct for patients suspected of having liver iron overload: can virtual iron content imaging accurately quantify liver iron content? *Radiology* 277:95–103
54. Dalbeth N, House ME, Aati O et al (2015) Urate crystal deposition in asymptomatic hyperuricaemia and symptomatic gout: a dual energy CT study. *Ann Rheum Dis* 74:908–911
55. Kim HR, Lee JH, Kim NR, Lee SH (2014) Detection of calcium pyrophosphate dihydrate crystal deposition disease by dual-energy computed tomography. *Korean J Intern Med* 29:404–405
56. Aggarwal A, Singbal SB, Yiew DSS, Tian QS, Wang S, Junwei Z (2019) Pigmented villonodular synovitis: novel role of dual-energy CT. *J Clin Rheumatol*. <https://doi.org/10.1097/rhu.0000000000000980>
57. Zheng S, Dong Y, Miao Y et al (2014) Differentiation of osteolytic metastases and Schmorl's nodes in cancer patients using dual-energy CT: advantage of spectral CT imaging. *Eur J Radiol* 83:1216–1221
58. Suh CH, Yun SJ, Jin W, Lee SH, Park SY, Ryu CW (2018) Diagnostic performance of dual-energy CT for the detection of bone marrow oedema: a systematic review and meta-analysis. *Eur Radiol* 28:4182–4194
59. Rajiah P, Sundaram M, Subhas N (2019) Dual-energy CT in musculoskeletal imaging: what is the role beyond gout? *AJR Am J Roentgenol* 213:493–505
60. Omoumi P, Verdun FR, Guggenberger R, Andreisek G, Becce F (2015) Dual-energy CT: basic principles, technical approaches,

- and applications in musculoskeletal imaging (part 2). *Semin Musculoskelet Radiol* 19:438–445
61. McNamara MM, Little MD, Alexander LF, Carroll LV, Beasley TM, Morgan DE (2015) Multireader evaluation of lesion conspicuity in small pancreatic adenocarcinomas: complimentary value of iodine material density and low keV simulated monoenergetic images using multiphasic rapid kVp-switching dual energy CT. *Abdom Imaging* 40:1230–1240
  62. Rizzo S, Femia M, Radice D et al (2018) Evaluation of deep myometrial invasion in endometrial cancer patients: is dual-energy CT an option? *Radiol Med* 123:13–19
  63. De Cecco CN, Caruso D, Schoepf UJ et al (2018) A noise-optimized virtual monoenergetic reconstruction algorithm improves the diagnostic accuracy of late hepatic arterial phase dual-energy CT for the detection of hypervascular liver lesions. *Eur Radiol*. <https://doi.org/10.1007/s00330-018-5313-6>
  64. Weiss J, Notohamiprodjo M, Bongers M et al (2017) Noise-optimized monoenergetic post-processing improves visualization of incidental pulmonary embolism in cancer patients undergoing single-pass dual-energy computed tomography. *Radiol Med* 122:280–287
  65. Qin L, Ma Z, Yan F, Yang W (2018) Iterative model reconstruction (IMR) algorithm for reduced radiation dose renal artery CT angiography with different tube voltage protocols. *Radiol Med* 123:83–90
  66. Sheafor DH, Kovacs MD, Burchett P, Picard MM, Davis B, Hardie AD (2018) Impact of low-kVp scan technique on oral contrast density at abdominopelvic CT. *Radiol Med* 123:918–925
  67. Bahrami-Motlagh H, Hassanian-Moghaddam H, Zamini H, Zamani N, Gachkar L (2018) Correlation of abdominopelvic computed tomography with clinical manifestations in methamphetamine body stuffers. *Radiol Med* 123:98–104
  68. Grimm J, Wudy R, Ziegeler E et al (2014) Differentiation of heroin and cocaine using dual-energy CT-an experimental study. *Int J Legal Med* 128:475–482
  69. Uyeda JW, Richardson IJ, Sodickson AD (2017) Making the invisible visible: improving conspicuity of noncalcified gallstones using dual-energy CT. *Abdom Radiol NY* 42:2933–2939
- Publisher's Note** Springer Nature remains neutral with regard to jurisdictional claims in published maps and institutional affiliations.